

# On the Temperature and Composition Dependence of Non-basal Stacking Faults in C14 Laves Phases

Zhuocheng Xie,\* Dimitri Chauraud, Erik Bitzek, Sandra Korte-Kerzel, and Julien Guénolé\*

Activation of non-basal slip is essential in improving the deformability of hexagonal crystals. However, for complex intermetallics such as Laves phase, the mechanism of non-basal slip remains largely unknown. In this work, the prismatic slip systems of C14 Laves phase crystals and possible metastable states along the slip paths are assessed using atomistic simulations. Multiple prismatic stacking fault states with the same projected positions of atoms but different site occupancies and chemical distributions are identified at different inter-atomic layers, temperatures and chemical compositions. The formation of energetically favorable prismatic stacking faults involves short-range diffusion which implies the thermally activated nature of prismatic slip. The outcomes of this work advance the understanding of temperature and composition-dependent non-basal slip in Laves phases.

## 1. Introduction

Laves phases are intermetallics that are present in various alloys and exert a significant influence on their mechanical characteristics due to their high strength and superior creep resistance in comparison to the matrix phases.<sup>[1–3]</sup> Despite their excellent mechanical performance at elevated temperatures, Laves phase alloys are commonly deemed unsuitable for structural applications

because of their well-known brittleness at room temperature.<sup>[3–5]</sup> Synchro-shear,<sup>[6,7]</sup> as the most energetically favorable mechanism of plasticity on basal or {111} planes in Laves phases, is widely studied, particularly using atomic-scale modeling.<sup>[8–10]</sup> Recently, the authors reported the mechanisms of motion of synchro-Shockley dislocations using atomistic simulations.<sup>[11,12]</sup> However, the mechanisms underlying plastic deformation on non-basal planes in hexagonal (or non-{111} planes in cubic) Laves phases are not well understood so far.

In the early 1970s, Paufler et al.<sup>[13,14]</sup> reported the activation of grown-in prismatic dislocations in the prototype C14 MgZn<sub>2</sub> under uniaxial compression at temperatures around 400 °C. Recently,


Zehnder et al.<sup>[15]</sup> investigated the plastic deformation of single crystal C14 CaMg<sub>2</sub> at room temperature by nanoindentation and microcompression. The prismatic slip was confirmed by slip trace analysis and exhibits the lowest critical resolved shear stress (CRSS) among basal and non-basal slip systems. Freund et al.<sup>[16]</sup> further investigated the activation of these slip systems of the CaMg<sub>2</sub> phase in the temperature range from 50 to 250 °C, where prismatic slip shows a decreasing CRSS with temperature. Zhang et al.<sup>[17]</sup> characterized two prismatic stacking fault (SF) structures with the same crystal lattice but different site occupancies in a C14 Nb-based Laves phase using atomic-resolution scanning transmission electron microscopy (STEM) after deformation in different temperature regimes. They interpreted the formation of high and room-temperature prismatic SFs based on the morphology of prismatic planes and topologically close-packing rules. The high-temperature SF formation was attributed to the diffusion-assisted shuffle mechanism, while the low-temperature SF formation was associated with the glide mechanism. In addition, the prismatic SFs were not flat and exhibited numerous steps, which was attributed to dislocation motion through frequent switching between different prismatic slip planes.

So far, the deformation mechanisms of prismatic plasticity in C14 Laves phases, particularly the formation of prismatic SFs by partial dislocation propagation, are still not well understood. In this study, we investigated the temperature and composition dependence of prismatic slip in C14 CaMg<sub>2</sub> and MgZn<sub>2</sub> Laves phases by performing atomistic simulations using semi-empirical potentials.<sup>[18,19]</sup> The minimum energy paths (MEPs) of slip events on different prismatic interlayers were identified

Z. Xie, S. Korte-Kerzel  
Institute of Physical Metallurgy and Materials Physics  
RWTH Aachen University  
52056 Aachen, Germany  
E-mail: xie@imm.rwth-aachen.de

D. Chauraud, E. Bitzek  
Max-Planck-Institut für Nachhaltige Materialien GmbH  
Max-Planck-Str. 1, 40237 Düsseldorf, Germany

J. Guénolé  
Arts et Métiers  
CNRS, Université de Lorraine  
LEM3, 57070 Metz, France  
E-mail: julien.guenole@univ-lorraine.fr

 The ORCID identification number(s) for the author(s) of this article can be found under <https://doi.org/10.1002/adem.202400885>.

© 2024 The Author(s). Advanced Engineering Materials published by Wiley-VCH GmbH. This is an open access article under the terms of the Creative Commons Attribution-NonCommercial License, which permits use, distribution and reproduction in any medium, provided the original work is properly cited and is not used for commercial purposes.

DOI: 10.1002/adem.202400885

using the nudged elastic band (NEB) method.<sup>[20,21]</sup> The effects of temperature and chemical composition on SF structures were studied using molecular dynamics (MD) and hybrid MD/Monte Carlo (MC)<sup>[22]</sup> simulations, respectively. The FIRE<sup>[23,24]</sup> and Quickmin<sup>[25]</sup> algorithms were used for relaxation in molecular statics (MS) simulations and NEB calculations, respectively. For more details on the simulation methods, see section 4.

## 2. Results and Discussion

### 2.1. Prismatic Slip Systems and Stacking Fault States

The prismatic slip systems were systematically assessed by calculating the generalized stacking fault energy ( $\gamma$ ) surfaces of

three possible interlayers on prismatic  $\{1100\}$  plane in C14  $\text{CaMg}_2$  (see Figure 1a,c,e) and  $\text{MgZn}_2$  (see Figure S1a,c,e, Supporting Information). *Meta*-stable states close to the  $[11\bar{2}0]$  slip paths were identified as the prismatic SF states in all interlayers. After full relaxation, the SF of interlayer III (SF III) shows the lowest stacking fault energy (SFE:  $422 \text{ mJ m}^{-2}$  in C14  $\text{CaMg}_2$  and  $265 \text{ mJ m}^{-2}$  in C14  $\text{MgZn}_2$ ), presumably more stable than the SF states of interlayer I and II (SF I and SF II), as summarized in Table 1. The energy barriers of full and partial slip paths were calculated using the NEB method as shown in Figure 1b,d,f. Although the interplanar distance of interlayer III is almost two times larger than interlayer I and II, the energy barriers of slip events on the three interlayers are at similar levels. For interlayer I and II, the energy barrier profiles are nearly identical. For the

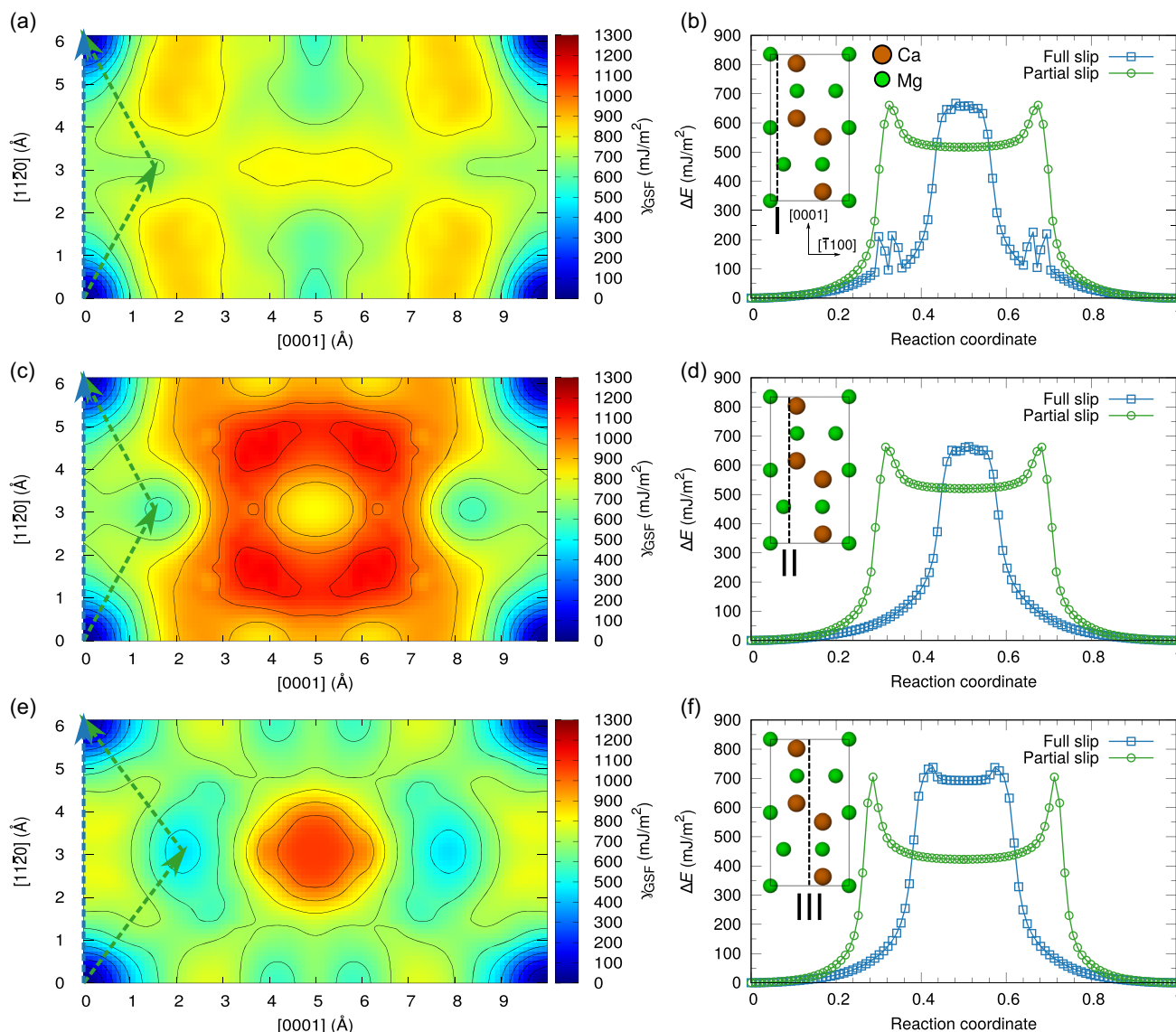


**Figure 1.** Prismatic slip systems of C14  $\text{CaMg}_2$ . Generalized stacking fault energy ( $\gamma$ ) surfaces of interlayer a) I, c) II, and e) III. Minimum energy paths computed for full ( $[11\bar{2}0]$  or  $\langle a \rangle$ ) and partial ( $\langle a + c \rangle$ ) slip events on interlayer b) I, d) II, and f) III using NEB. The full and partial slip directions are marked in blue and green dashed arrows on the  $\gamma$  surfaces, respectively. The C14 unit cell and prismatic slip planes (marked in black dashed lines) are shown in the insets. Ca (large) and Mg (small) atoms are colored brown and green, respectively.

**Table 1.** Summary of interplanar distances of prismatic interlayers, the energy barriers of full ( $\Delta E_{\text{full}}$ ) and partial ( $\Delta E_{\text{partial}}$ ) slip paths on prismatic planes and prismatic stacking fault energies (SFE) of C14  $\text{CaMg}_2$  and  $\text{MgZn}_2$  and SFE of optimized prismatic stacking fault structures.

Interlayer	$\text{CaMg}_2$			$\text{MgZn}_2$		
	I	II	III	I	II	III
Interplanar distance [Å]	0.902	0.871	1.712	0.760	0.731	1.433
$\Delta E_{\text{full}}$ [mJ m <sup>-2</sup> ]	667	664	738	495	495	512
$\Delta E_{\text{partial}}$ [mJ m <sup>-2</sup> ]	661	662	705	476	476	420
SFE [mJ m <sup>-2</sup> ]	516	516	422	460	460	265
Optimized SFE [mJ m <sup>-2</sup> ]	374	374	326	191	191	189

full slip paths, the energy barriers on interlayer III are 11% and 3% higher than on interlayer I/II in C14  $\text{CaMg}_2$  and  $\text{MgZn}_2$ , respectively. For the partial slip paths, the energy barriers on interlayer III are 7% higher and 12% lower than on interlayer I/II in C14  $\text{CaMg}_2$  and  $\text{MgZn}_2$ , respectively. Additionally, the energy barrier for partial slip paths within the same interlayer is slightly lower compared to that of full slip paths.

The identification of prismatic SF states is in agreement with the experimental observation in a C14 Nb-based Laves phase after low and high-temperature deformation by Zhang et al.<sup>[17]</sup> Abundant extended prismatic SFs bounded by partial dislocations with compact cores and Burgers vectors of  $\frac{3}{16}[0001] + \frac{1}{6}[11\bar{2}0]$  were observed in atomic-resolution STEM.<sup>[17]</sup> Our study determined the Burgers vectors of prismatic partial slip close to  $\frac{3}{16}[0001] + \frac{1}{6}[11\bar{2}0]$ , which correlates well with the aforementioned experimental results. Furthermore, Zhang et al.<sup>[17]</sup> reported that the prismatic SF is not flat and exhibits numerous steps, which they attributed to the movement of dislocations frequently switching between different prismatic slip planes. This can be explained by the nearly equal energy barriers we calculated for prismatic slip paths on interlayer I, II, and III, see Table 1. Further research is needed to gain a more comprehensive understanding of the out-of-plane mechanisms of prismatic dislocations switching between various interlayers and the associated energy barriers.

Three prismatic SF states with different microstructures and energies were found in this work (see Figure 2a–c). The structures of SF I and II (of interlayers I and II, respectively) demonstrate rotational symmetry (a 180° rotation around the axis aligned with the viewing direction) and therefore exhibit the same SFE. The arrangement of atoms within the SF consisting of a Laves building block (marked in blue dashed rhombic tile) with the characteristic triple-layer and a  $\text{Zr}_4\text{Al}_3$  building block (marked in blue dashed rectangular tile) was found in SF I and II. This fundamental building block also exists in the  $\mu$ -phase. Note that an empty site in the  $\text{Zr}_4\text{Al}_3$  building block was observed, see Figure 2a,b. A similar arrangement of atoms exists in SF III, with different site occupancies and chemical distributions (see Figure 2c). In this case, an empty site exists in the middle atomic column of the Laves building block. Interestingly, these SF structures are not thermally stable at room or elevated

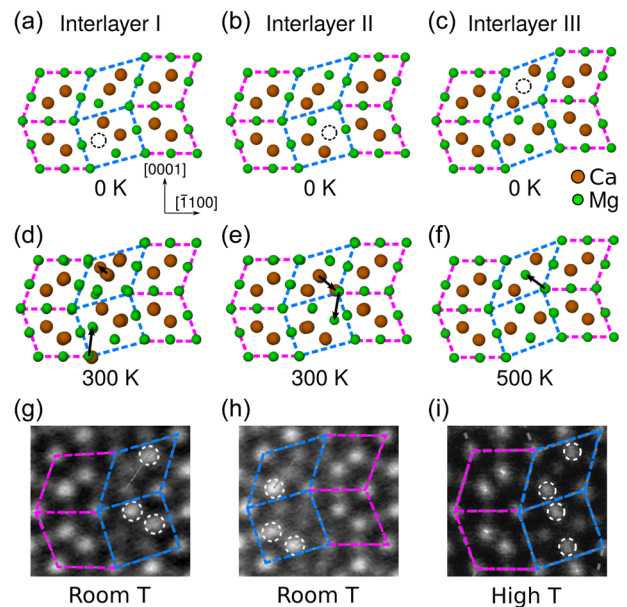


**Figure 2.** Prismatic stacking faults in C14  $\text{CaMg}_2$ . Stacking faults of interlayer a) I, b) II, and c) III after energy minimization (force tolerance:  $10^{-8}$  eV Å<sup>-1</sup>). Stacking fault configurations were equilibrated for 200 ps at finite temperatures in isothermal-isobaric (NPT) ensemble using MD simulations: interlayer d) I and e) II at 300 K and f) interlayer III at 500 K. The black arrows indicate the atomic displacement relative to the configurations at 0 K. The black dashed circles indicate the empty sites. Ca (large) and Mg (small) atoms are colored brown and green, respectively. Blue and magenta dashed tiles indicate the prismatic stacking fault and perfect lattices, respectively. Prismatic stacking fault structures in C14 Nb(Cr, Ni, Al)<sub>2</sub> Laves phase after g,h) room temperature impact deformation and i) high-temperature compression. The white dashed circles indicate the sites with high intensity. (g–i) Adapted with permission.<sup>[17]</sup> Copyright, American Physical Society.

temperature. After equilibration at 300 K, a structural transition induced by short-range diffusion was observed in SF I and II. The empty site is partially occupied by small (Mg) atoms hopping from a nearby site at the junction of four lattice tiles, and the large (Ca) atoms in the middle atomic column of the Laves building block shift toward the site where the small atoms are left behind, see Figure 2d,e. The structure of SF I and II at 300 K is very similar to the experimentally observed prismatic SF structures after room temperature deformation in ref [17], see Figure 2g,h. In addition to the identical lattice tiles, the atomic distributions in SFs are similar in our atomic configurations and high-resolution STEM images. The positions of three bright atomic columns (highlighted using white dashed circles) corresponding to the heavy elements (Nb in Nb-base Laves phase) correlate well with the simulation results (Ca in C14  $\text{CaMg}_2$ ). In addition, the shift of the middle atomic column out of the Laves triple-layer was also reported in the experiment as illustrated using the grey dashed line in Figure 2g,h.

SF III shows better thermal stability than SF I and II. It keeps the same atomic structure at 300 K with a structural transition observed after equilibration at 500 K only, see Figure 2c,f. The empty site in the Laves building block is partially occupied by

small (Mg) atoms hopping from a nearby site at the junction of lattice tiles. Compared to the SF observed in experiments following high-temperature deformation, diffusion-assisted SF III at 500 K exhibits a similar chemical distribution in the Laves building block but a distinct chemical distribution in the  $Zr_4Al_3$  building block. In the experimental observation, the heavy (large) atoms are positioned at the up and down sites within the  $Zr_4Al_3$  building block (Figure 2i), whereas in the MD simulation, they are situated at the left and right sites (Figure 2f). These discrepancies between the 0 K SF structures obtained in the  $\gamma$  surface calculations and the experimentally observed SF structures after finite temperature deformation imply that the formation of prismatic SF involves not only simple crystallographic slip mechanisms but also diffusion, highlighting the thermally activated nature of prismatic slip. More detailed interpretations of

the temperature-dependent mechanisms of partial slip events and their correlation with the experimental SF structures are presented in the next subsection.

## 2.2. Mechanisms of Partial Slip Events

According to our calculations, the atomic displacement introduced by thermalization at room temperature optimizes the structure of glide-induced SF I and II by shifting one out of two atoms in the Mg atomic column to the empty site (see the displacement vectors as shown in the inset of Figure 3a). After energy minimization, the Ca atoms located in the atomic column in the Laves triple-layer shift toward the empty site left behind by the Mg atoms. The SFE of SF I decreases by 28% to

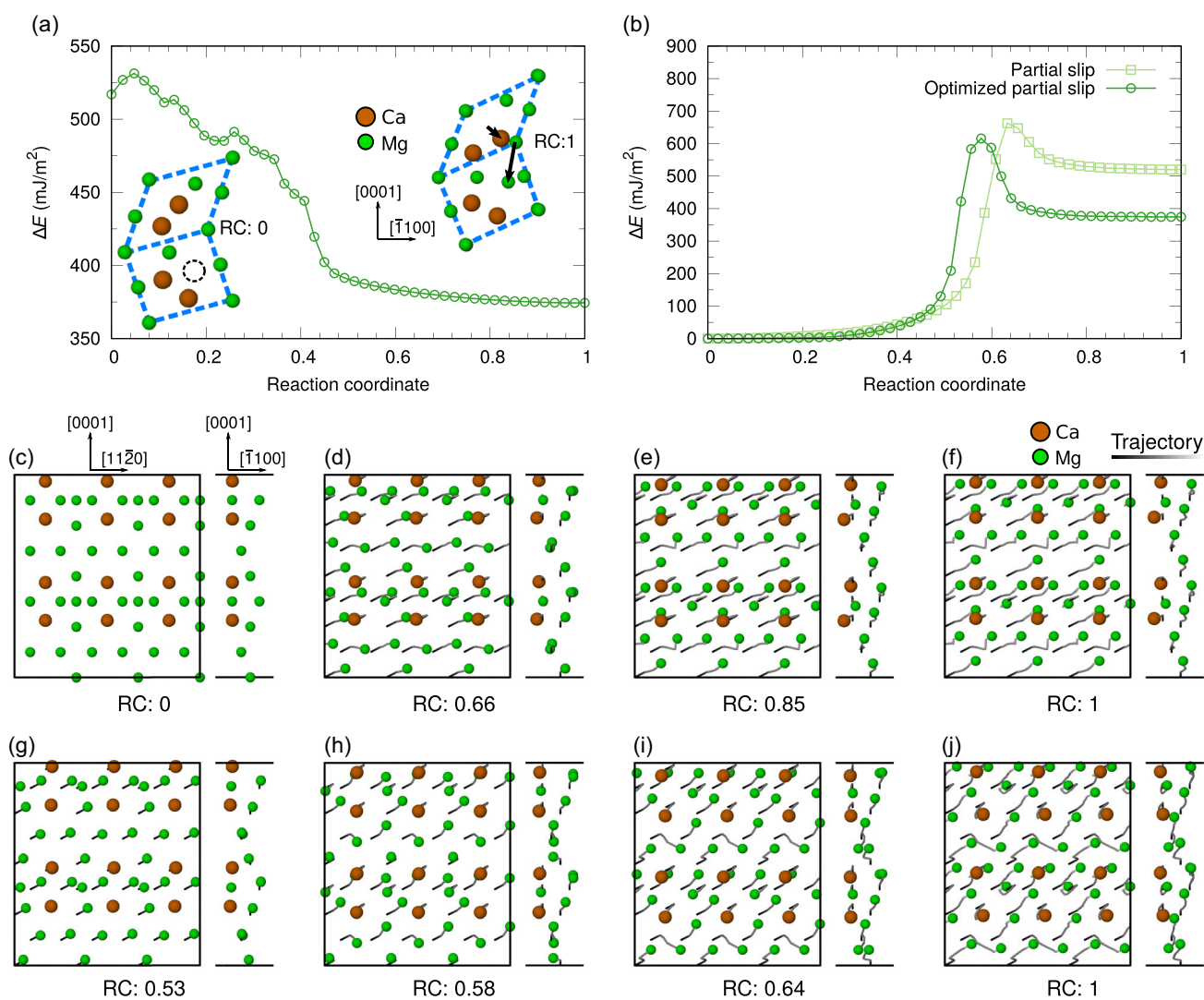


**Figure 3.** Mechanisms of partial slip events and formation of stacking fault I/II at interlayer I/II in C14 CaMg<sub>2</sub>. a) Minimum energy path computed for the transition from glide-induced SF I to diffusion-assisted SF I using NEB. The insets show the stacking fault structures at reaction coordinates (RC) 0 and 1. The black arrows indicate the atomic displacement relative to RC 0. The dashed circle indicates the empty site. b) Minimum energy path computed for the partial slip event and optimized partial slip event using NEB. c–f) Transition states of the partial slip event. g–j) Transition states of the optimized partial slip event. Left: view along  $[\bar{1}100]$  direction; right: view along  $[11\bar{2}0]$  direction. Ca (large) and Mg (small) atoms are colored brown and green, respectively. Trajectories of atoms are colored in a black-grey gradient according to the reaction coordinate.



374 mJ m<sup>-2</sup> in CaMg<sub>2</sub>, and by 58% to 191 mJ m<sup>-2</sup> in MgZn<sub>2</sub> after the structural optimization. The NEB calculation was performed to find the MEP between the initial and optimized SF states (see Figure 3a). For the glide-induced SF I and II, a small energy barrier of 15 mJ m<sup>-2</sup> could be overcome with thermally assisted diffusion to reach a SF state with lower energy. In addition to a lower SFE, the diffusion-assisted formation of SF I and II states (Figure 3b) is mediated by a different mechanism (Figure 3c–j) with a lower energy barrier. Simple crystallographic slip mediates the partial slip events between the pristine and glide-induced SF I and II states, with all atoms moving in the same direction as the partial Burgers vector (as illustrated in Figure 3c–f). For the partial slip event between the pristine and optimized SF I and II states, a synchroshear-like mechanism was identified, where certain Mg atoms move in a direction that differs from the direction of the partial Burgers vector.

The structure of glide-induced SF III is optimized by swapping the elemental type in the Zr<sub>4</sub>Al<sub>3</sub> building block to be identical as reported in the experiment (see Figure S2c,d, Supporting Information). The SFE of the optimized SF III after the swapping decreases to 326 (by 23%) and 189 (by 29%) mJ m<sup>-2</sup> in CaMg<sub>2</sub> and MgZn<sub>2</sub>, respectively. After atomic swapping within the SF III structure, site occupancies adhere to the principles of topologically close packing, namely larger atoms (denoted as A in the AB<sub>2</sub> formula) occupy larger sites (identified as Z15 and Z16 according to the classification by Frank and Kasper<sup>[26,27]</sup>) and smaller atoms (B in AB<sub>2</sub>) occupy smaller sites (Z12 and Z14). The formation of the more energetically favorable SF III state necessitates a more substantial thermal fluctuation than the optimized SF I and II state due to its involvement in not only atomic diffusion but also atomic swapping. This rationalizes the experimental evidence of optimized SF III that is mainly observed after high temperature deformation.<sup>[17]</sup>

The formation of more energetically favorable prismatic SFs requires the assistance of diffusion implies the strong thermally

activated nature of prismatic partial dislocations. Thermal assistance was demonstrated to be indispensable in activating synchro-Shockley dislocations, implying that the motion of this zonal dislocation is prohibited at low temperatures.<sup>[11,12]</sup> A temperature-dependent deformation behavior is also expected for prismatic partial dislocations where the thermal fluctuation can significantly lower not only the planar fault energies but also the associated energy barriers of slip events.

### 2.3. Composition Dependence of Site Occupancy

The composition-dependent prismatic SF III structures in C14 MgZn<sub>2</sub> were investigated using hybrid MD/MC in the variance-constrained semi-grand canonical (VC-SGC) ensemble at 500 K. The SF I and II structures in C14 MgZn<sub>2</sub> exhibit instability at elevated temperatures, attributed to the very small energy differences between the SF states and the subsequent energy maxima (see Figure S1b,d, Supporting Information). The target concentrations were set within the range of 5% off-stoichiometry, that is from 28.3% to 38.3% Mg. After reaching equilibrium, the site occupancy intensity  $N_A/N_{\text{tot}}$  (where  $N_A$  is the number of A-type atoms and  $N_{\text{tot}}$  represents the total number of sites within a single atomic column in AB<sub>2</sub> Laves phase) was averaged over all unit cells within the prismatic SFs. The statistics of the site occupancies in SF III at different chemical compositions are shown in Figure 4f and the Frank-Kasper naming convention of the sites is illustrated in Figure 4e. Multiple SF III states with different chemical compositions are depicted in the chemical distribution schematic of Figure 4a–d. As compared to the matrix, a significantly higher concentration of solute atoms was identified at prismatic SFs after 16 000 MC steps (1.6 ns MD time), see Figure S3, Supporting Information. The atomic swapping mainly takes place in the Zr<sub>4</sub>Al<sub>3</sub> building blocks, with the Laves building blocks that remain unchanged except at 28.3% Mg

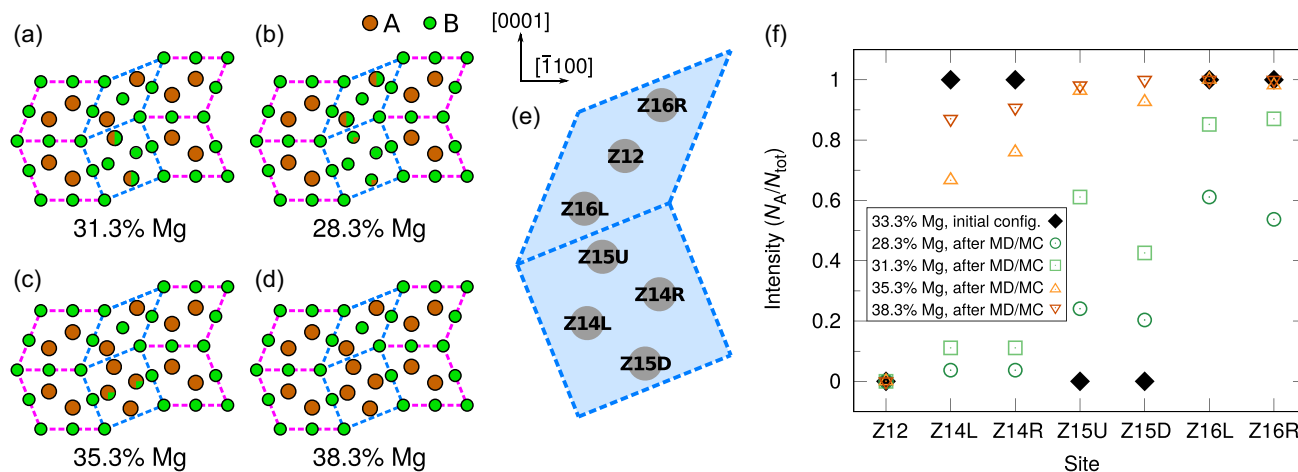


**Figure 4.** Prismatic stacking fault III in C14 MgZn<sub>2</sub> at 500 K and off-stoichiometric compositions. a–d) Schematic of chemical distribution in the SF III under different target Mg concentrations after 1.6 ns hybrid MD/MC simulations (1 MC step with 10% swap fraction every 0.1 ps MD time) in variance-constrained semi-grand canonical (VC-SGC) ensemble ( $T = 500$  K,  $\kappa = 1000$ ,  $\Delta\mu = \pm 0.3$  eV). Mg (large) and Zn (small) atoms are colored brown and green, respectively. For the atomic sites with two colors, the fraction of the area represents the rough estimation of the percentage of the element in one atomic column. f) The schematic illustration of the atomic arrangement in prismatic stacking fault. The atomic site is named after the type of surrounding atomic cluster (i.e., Z12 indicates the site is the center of an icosahedral cluster) and corresponding position (i.e., L: left; R: right; U: up; D: down) in the tiles. e) The intensity of A-type atom (for AB<sub>2</sub> Laves phase) in an atomic column of the stacking fault sites.

composition. At 31.3% Mg composition (−2% off-stoichiometry), Z14L and Z14R are nearly fully occupied by Zn (small) atoms in contrast to the glide-induced SF III configuration (Figure 2f). In addition, half of the Z15U and Z15D sites are occupied by Mg (large) atoms. With decreasing Mg content, around 75% Z15U and Z15D sites are occupied by Zn atoms at 28.3% Mg composition. On the Mg-rich side of the off-stoichiometry, all sites in the  $\text{Zr}_4\text{Al}_3$  building blocks are mostly occupied by Mg atoms. At 38.3% Mg composition (+5% off-stoichiometry), nearly pure Mg  $\text{Zr}_4\text{Al}_3$  building blocks were obtained. The variation in local chemical distribution within SF III at differing chemical compositions offers a potential explanation for the observed variance in the intensity of atomic columns at identical sites across various unit cells along the prismatic SF in the room-temperature impact sample, as reported by Zhang et al.<sup>[17]</sup> The presence of diverse prismatic SF states in off-stoichiometry implies that the chemical composition has an impact on prismatic plasticity. To gain a more profound comprehension of prismatic plasticity, additional works are necessary, such as unraveling dislocation mechanisms and the effects of solute atoms on dislocation motion.

### 3. Conclusion

In this study, we evaluated the prismatic slip systems and potential metastable states of C14  $\text{CaMg}_2$  and  $\text{MgZn}_2$  using atomistic simulations. Various prismatic stacking fault states with identical projected positions of atoms but different chemical distributions and site occupancies were identified at varying interlayers, temperatures and chemical compositions. These enlighten atomically resolved experimental observations previously reported in the literature. The formation of prismatic stacking faults that are energetically favorable involves short-range diffusion, indicating that prismatic slip is thermally activated. The findings of this work enhance our comprehension of non-basal slip in Laves phases, which is known to be dependent on temperature and chemical composition.<sup>[16,28]</sup>

### 4. Simulation Methods

The atomistic simulations were performed using the molecular dynamics (MD) software package LAMMPS.<sup>[29]</sup> The interatomic interactions were modeled by the modified embedded atom method (MEAM) potential by Kim et al.<sup>[18]</sup> for Ca-Mg and the embedded atom method (EAM) potential by Brommer et al.<sup>[19]</sup> for the Mg-Zn system. Both potentials reasonably describe the mechanical properties of C14  $\text{CaMg}_2$  and  $\text{MgZn}_2$  Laves phases as compared to experiments and ab initio calculations (see Table S1, Supporting Information).

To investigate the prismatic  $\{\bar{1}100\}$  slip systems, the C14  $\text{CaMg}_2$  and  $\text{MgZn}_2$  Laves structures were constructed using AtomsK<sup>[30]</sup> following the crystallographic orientation:  $x = [1120]$ ,  $y = [\bar{1}100]$  and  $z = [0001]$ . Generalized stacking fault energy (GSFE) surfaces were calculated by incrementally shifting one-half of the crystal along the slip directions across the slip plane. Periodic boundary conditions (PBC) were applied in the  $x$  and  $z$  directions parallel to the slip plane (contains  $3 \times 2$  unit cells). Non-periodic

boundary conditions were used along the  $y$ - $[\bar{1}100]$  direction (20 unit cells in  $y$ -direction). The FIRE<sup>[23,24]</sup> algorithm with the force tolerance of  $10^{-8} \text{ eV } \text{\AA}^{-1}$  was used to relax atoms along the  $y$ - $[\bar{1}100]$  direction after each displacement step. The energy barrier  $\Delta E$  was calculated according to Equation (1):

$$\Delta E = \frac{E - E_0}{A} \quad (1)$$

where  $E_0$  is the energy of the initial configuration before rigid-body displacement and  $A$  is the area of slip plane  $A = l_x l_z$ . The stacking fault states were identified on the GSFE surfaces and then fully relaxed. Convergence tests of the dimensions of the simulation box on the prismatic SFE were performed and demonstrated that  $3 \times 20 \times 2$  unit cells are sufficient to accurately capture SFE and ensure reliable simulation results, see Figure S4, Supporting Information. In addition, climbing image nudged elastic band (NEB)<sup>[20,21]</sup> calculations were performed to find saddle points and minimum energy paths (MEPs) of slip events on the atomic configurations with the same dimensions and boundary conditions as above mentioned. The spring constants for parallel and perpendicular nudging forces are both  $1.0 \text{ eV } \text{\AA}^{-2}$ . Quickmin<sup>[25]</sup> was used to minimize the energies across all replicas until the force norm was below  $0.01 \text{ eV } \text{\AA}^{-1}$ .

The prismatic stacking fault configurations ( $9 \times 40 \times 6$  unit cells with PBC in all directions) in C14  $\text{CaMg}_2$  and  $\text{MgZn}_2$  were equilibrated for 200 ps at 300 or 500 K using the Nosé–Hoover thermostat together with the Nosé–Hoover barostat<sup>[31]</sup> to relax possible stresses. The timestep is 1 fs. To investigate the chemical distribution at planar faults, hybrid MD/Monte Carlo (MC) simulations in the variance-constrained semi-grand canonical (VC-SGC)<sup>[22]</sup> ensemble ( $\kappa = 1000$ ,  $\Delta\mu = \pm 0.3 \text{ eV}$ ) were performed at  $T = 500 \text{ K}$  on the C14  $\text{MgZn}_2$  sample containing prismatic stacking faults for 1.6 ns (1 MC step with 10% swap fraction every 0.1 ps MD time). The target concentrations of Mg atoms vary from 28.3% to 38.3% ( $\pm 5\%$  off-stoichiometry). The  $\Delta\mu$  values were derived by optimizing the number of successful atomic swaps to achieve the desired concentration after 20 iterations. At 500 K, within a  $\pm 5\%$  chemical concentration range, the optimized  $\Delta\mu$  values were determined to be within the range of  $-0.26$ – $0.33 \text{ eV}$ . To ensure that the systems reach equilibrium at the target concentration, chemical potential and temperature, we used the evolution of potential energies (Figure S5, Supporting Information), local and global concentrations (Figure S6, Supporting Information), and successful swap rates (Figure S7, Supporting Information) as indicators.

The atomic structures were quenched using the conjugate gradient method to reduce thermal noise for visualization. The Open Visualization Tool (OVITO)<sup>[32]</sup> was used to visualize the atomic configurations and trajectories.

### Supporting Information

Supporting Information is available from the Wiley Online Library or from the author.

### Acknowledgements

The authors acknowledge financial support by the Deutsche Forschungsgemeinschaft (DFG) through the projects A02, A05, and

C02 of the SFB1394 Structural and Chemical Atomic Complexity – From Defect Phase Diagrams to Material Properties, project ID 409476157. This project has received funding from the European Research Council (ERC) under the European Union's Horizon 2020 research and innovation programme (grant agreement no. 852096 FunBlocks). Simulations were performed with computing resources granted by RWTH Aachen University under project (p0020267) and by the EXPLOR center of the Université de Lorraine and by the GENCI-TGCC (grant no. 2020-A0080911390). The authors would like to thank Peter Brommer (University of Warwick) for his assistance in converting the EAM potential to the DYNAMO format.

Open Access funding enabled and organized by Projekt DEAL.

## Conflict of Interest

The authors declare no conflict of interest.

## Data Availability Statement

The data that support the findings of this study are openly available in [Zenodo] at [https://doi.org/10.5281/zenodo.10948157], reference number [10948157].

## Keywords

atomistic simulation, laves phase, prismatic slip, stacking fault

Received: April 11, 2024

Revised: June 17, 2024

Published online:

- [1] A. K. Sinha, *Prog. Mater. Sci.* **1972**, 15, 81.
- [2] P. Paufler, *Intermetallics* **2011**, 19, 599.
- [3] F. Stein, A. Leineweber, *J. Mater. Sci.* **2021**, 56, 5321.
- [4] J. Livingston, *Phys. Status Solidi A* **1992**, 131, 415.
- [5] T. M. Pollock, *Science* **2010**, 328, 986.
- [6] M. Kronberg, *Acta Metall.* **1957**, 5, 507.
- [7] M. F. Chisholm, S. Kumar, P. Hazzledine, *Science* **2005**, 307, 701.
- [8] O. Vedmedenko, F. Rösch, C. Elsässer, *Acta Mater.* **2008**, 56, 4984.
- [9] J. Guérolé, F.-Z. Mouhib, L. Huber, B. Grabowski, S. Korte-Kerzel, *Scr. Mater.* **2019**, 166, 134.

- [10] W. Luo, Z. Xie, S. Zhang, J. Guérolé, P.-L. Sun, A. Meingast, A. Alhassan, X. Zhou, F. Stein, L. Pizzagalli, B. Berkels, *Adv. Mater.* **2023**, 35, 2300586.
- [11] Z. Xie, D. Chauraud, A. Atila, E. Bitzek, S. Korte-Kerzel, J. Guérolé, *Phys. Rev. Mater.* **2023**, 7, 053605.
- [12] Z. Xie, D. Chauraud, A. Atila, E. Bitzek, S. Korte-Kerzel, J. Guérolé, *Scr. Mater.* **2023**, 235, 115588.
- [13] P. Paufler, J. Marschner, G. Schulze, *Phys. Status Solidi B* **1970**, 40, 573.
- [14] H. Kubsch, P. Paufler, G. Schulze, *Phys. Status Solidi A* **1974**, 25, 269.
- [15] C. Zehnder, K. Czerwinski, K. D. Molodov, S. Sandlöbes-Haut, J. S.-L. Gibson, S. Korte-Kerzel, *Mater. Sci. Eng., A* **2019**, 759, 754.
- [16] M. Freund, D. Andre, C. Zehnder, H. Rempel, D. Gerber, M. Zubair, S. Sandlöbes-Haut, J. S.-L. Gibson, S. Korte-Kerzel, *Materialia* **2021**, 20, 101237.
- [17] Y. Zhang, W. Zhang, B. Du, W. Li, L. Sheng, H. Ye, K. Du, *Phys. Rev. B* **2020**, 102, 134117.
- [18] K.-H. Kim, J. B. Jeon, B.-J. Lee, *Calphad* **2015**, 48, 27.
- [19] P. Brommer, M. D. Boissieu, H. Euchner, S. Francoual, F. Gähler, M. Johnson, K. Parlinski, K. Schmalzl, *Z. Kristallogr. - Cryst. Mater.* **2009**, 224, 97.
- [20] G. Henkelman, B. P. Uberuaga, H. Jónsson, *J. Chem. Phys.* **2000**, 113, 9901.
- [21] G. Henkelman, H. Jónsson, *J. Chem. Phys.* **2000**, 113, 9978.
- [22] B. Sadigh, P. Erhart, A. Stukowski, A. Caro, E. Martinez, L. Zepeda-Ruiz, *Phys. Rev. B* **2012**, 85, 184203.
- [23] E. Bitzek, P. Koskinen, F. Gähler, M. Moseler, P. Gumbsch, *Phys. Rev. Lett.* **2006**, 97, 170201.
- [24] J. Guérolé, W. G. Nöhring, A. Vaid, F. Houllé, Z. Xie, A. Prakash, E. Bitzek, *Comput. Mater. Sci.* **2020**, 175, 109584.
- [25] D. Sheppard, R. Terrell, G. Henkelman, *J. Chem. Phys.* **2008**, 128, 134106.
- [26] F. C. Frank, J. S. Kasper, *Acta Crystallogr.* **1958**, 11, 184.
- [27] F. C. Frank, J. S. Kasper, *Acta Crystallogr.* **1959**, 12, 483.
- [28] M. Freund, Z. Xie, P.-L. Sun, L. Berners, J. Spille, H. Wang, C. Thomas, M. Feuerbacher, M. Lipinska-Chwalek, J. Mayer, S. Korte-Kerzel, *Acta Mater.* **2024**, 120124.
- [29] A. P. Thompson, H. M. Aktulga, R. Berger, D. S. Bolintineanu, W. M. Brown, P. S. Crozier, P. J. in 't Veld, A. Kohlmeyer, S. G. Moore, T. D. Nguyen, R. Shan, M. J. Stevens, J. Tranchida, C. Trott, S. J. Plimpton, *Comput. Phys. Commun.* **2022**, 271, 108171.
- [30] P. Hirel, *Comput. Phys. Commun.* **2015**, 197, 212.
- [31] W. G. Hoover, *Phys. Rev. A* **1985**, 31, 1695.
- [32] A. Stukowski, *Modell. Simul. Mater. Sci. Eng.* **2009**, 18, 015012.